

Chapter 2

A bifurcation study of double-diffusive flows

In this chapter the double diffusive layer formation process in a laterally heated liquid layer which is stably stratified through a constant vertical salinity gradient is considered. We focus on the situation for which the salt field is fixed at the upper and lower boundaries to allow for steady state solutions. The initial layer formation, subsequent layer merging and the long time evolution are considered from a dynamical systems point of view. The structure of the stationary solutions in parameter space and their linear stability is determined using continuation methods whereas transient flows are studied through direct numerical simulation. An attempt is made to identify the boundaries between different flow regimes, as observed experimentally, as paths of particular bifurcation points in parameter space. This is only partly successful due to an abundance of singularities in some parameter regimes. However, much is learned on the dynamics of these type of flows during the attempt. For instance, the evolution towards stable states at selective points in parameter space shows that unstable steady states are physically relevant because the time at which the particular instability sets in may be very long.

2.1 Introduction

When a lateral temperature gradient is applied to a motionless liquid layer which is stably stratified through a constant vertical salinity gradient ϕ_0 , a buoyancy driven flow appears. This flow may become unstable when a critical value of the lateral temperature gradient is exceeded. The instabilities are shear driven for small ϕ_0 , but when ϕ_0 is large the flow becomes unstable to

double diffusive instabilities. The latter are due to the different thermal and solutal diffusivities. A parcel of liquid near the hot vertical wall is heated and moves upward, retaining almost all of its salt due to the relatively small saline diffusivity. As the parcel rises, the background salinity stratification causes the lateral density difference between the parcel and the bulk of the fluid to decrease. The vertical excursion is limited to the height where the parcel density is equal to that of the surrounding liquid and because of continuity it is then forced to move laterally; a layered flow pattern results.

The vertical temperature and salinity structure associated with these layers show characteristic step-like structures. Such step structures in temperature and salinity have been found over large areas in the upper ocean. Since the presence of layers significantly influences the transport of heat and salt, double diffusive convection is a potentially important transport mechanism e.g. for heat and salt in the ocean [Schmitt, 1994]. Apart from the oceanographic context, there are many technological motivations to study these types of flow, for example crystal growth [Fernando and Brandt, 1995] and heat storage in solar ponds [Akbarzadeh and Manins, 1988].

Much information on the layer formation process was obtained from laboratory experiments. These were performed either in narrow slots or in wide tanks. They differ also in the way the heating is imposed at the lateral walls, for example very slowly [Thorpe *et al.*, 1969] or through a particular time dependence [Chen *et al.*, 1971; Tanny and Tsinober, 1988; Wirtz *et al.*, 1972]. In most of the experiments three stages of flow development are observed. There is an initial stage characterized either by spontaneous cell formation along the heated wall or by flow developing from the horizontal boundaries. In the latter flows, the cells at the horizontal boundaries penetrate towards the center of the cavity during the second stage of evolution. In the first type of flows, layers merge during the second stage leading to an increase in the average thickness of the layers. Eventually, in both cases, a quasi-steady pattern forms with a layered structure over the whole container. Nice sets of pictures showing these three stages can, for example, be found in Tanny and Tsinober [1988].

The experiments indicate that there is a boundary in parameter space separating these two qualitatively different regimes of flow. In Chen *et al.* [1971], a boundary in parameter space was proposed as the critical value of a Rayleigh number Ra_η based on the length scale

$$\eta = \frac{\alpha \Delta T}{\beta \phi_0} \tag{2.1}$$

Here ΔT is the laterally imposed temperature difference and α, β the thermal and solutal expansion coefficients, respectively. The length scale η is directly related to the movement of a heated liquid parcel to its neutrally buoyant level. It was found [Chen *et al.*, 1971] that when Ra_η exceeds a critical value given approximately by $Ra_{\eta,cr} = 1.5 \cdot 10^4$ the layers formed si-

2.1. Introduction

multaneously. In this case, a layered convection pattern with a vertical lengthscale η developed [Huppert and Turner, 1980; Jeevaraj and Imberger, 1991; Tanny and Tsinober, 1988]. Below the critical value the layers grow successively from the horizontal walls and layers with a larger scale may develop.

Theoretical work has mainly focussed on the initial stage of layer formation as an instability of a weak buoyancy driven background flow. In the ideal situation of a vertically unbounded layer this flow is parallel, with liquid rising near the hot wall and descending along the cold wall. The parallel flow can be calculated analytically [Thangam *et al.*, 1981] and at large salinity gradient ϕ_0 , it can be shown to be unstable to double diffusive instabilities for sufficiently large lateral temperature gradient. A rigorous series of studies on the instability of the boundary layer due to a gradually heated wall has been performed by Kerr [1989, 1990]. He demonstrated that for this case, the instability is oscillatory and that finite amplitude flows exist below the instability boundary (although these were found to be unstable).

In this chapter, we focus on the long time behavior of double diffusive layered flows in a narrow slot. The question we try to answer is whether the different flow regimes are related to a change in attractive regions in phase space of the governing system of equations. In that respect, the experimental results in Lee *et al.* [1990] and numerical results in Lee and Hyun [1991] are most relevant. In Lee *et al.* [1990], an experimental configuration was used for which the salt field at the horizontal walls was kept constant by using permeable membranes, maintaining a salinity difference ΔS between the walls. Here, real steady equilibria exist and can be calculated numerically in parameter space by solving for the steady equations directly. Apart from the above mentioned type of flows, which they called simultaneously formed layer flows (regime III) and successively formed layer flows (regime II), they also found two other regimes. At low buoyancy ratio¹ $R = \frac{\beta \Delta S}{\alpha \Delta T}$, a unicellular flow pattern was found (regime IV) and at very large buoyancy ratio, a very weak flow (or no flow at all) was found (regime I).

In addition to the aspect-ratio A of the liquid layer (ratio of length to depth), the Prandtl number and the Lewis number, two other parameters control the dynamics of the flow. These are the thermal Rayleigh number Ra_T based on the liquid height H (or Ra_η based on η) and the above mentioned buoyancy ratio R . The solutal Rayleigh number Ra_S is the product of Ra_T and R . The aspect-ratio, the Prandtl number and the Lewis number will be fixed throughout this study. The salt boundary conditions at the horizontal walls are chosen to allow for steady states to exist (as in Lee *et al.* [1990]). We use techniques from numerical bifurcation theory to determine branches of steady solutions in the two-dimensional parameter space spanned by Ra_η

¹In literature, different symbols and definitions exist for the buoyancy ratio, a fact which may lead to some confusion. In this thesis, the symbol R is used for the buoyancy ratio based on the *horizontal* background temperature difference ΔT . The commonly used symbol R_ρ is reserved for the vertical buoyancy (stability) ratio as used in Chapter 4.

and the buoyancy ratio R . In addition, some trajectories showing the evolution of the flow are computed by direct numerical simulation at particular locations in parameter space.

Main aim of this chapter is to identify the boundaries between the different flow regimes as paths of particular bifurcation points in parameter space. The work leads to the stability boundary of the weak buoyancy driven nonparallel flow; this is a symmetry breaking bifurcation point. A lower bound for the successively layered flow regime is likely to be associated with a path of limit points on the asymmetric branch originating from this symmetry breaking bifurcation. The boundary between the unicellular flow regime and that of the simultaneously formed layer regime is associated with the instability of the unicellular flow. Further identification could not be made due to an abundance of bifurcation points in several regions of parameter space.

2.2 Formulation and Numerical Methods

A two-dimensional rectangular container (length L and height H) is filled with a Newtonian liquid with a constant thermal diffusivity κ_T and kinematic viscosity ν . A stable vertical salinity gradient is maintained within the liquid by imposing a constant salinity difference ΔS between the horizontal walls of the container; the vertical heat flux at these walls vanishes. A constant horizontal temperature difference ΔT is applied between the vertical walls, which are impervious to salt. The density ρ depends linearly on temperature and salinity and is given by $\rho = \rho_0(1 - \alpha(T^* - T_0) + \beta(S^* - S_0))$, where the zero subscript refers to reference values. The governing equations are non-dimensionalized using scales H , H^2/κ_T and κ_T/H for length, time and velocity, respectively. A dimensionless temperature T and salinity S are defined by $T = (T^* - T_0)/\Delta T$ and $S = (S^* - S_0)/\Delta S$. In terms of the streamfunction ψ and vorticity ω , where

$$u = \frac{\partial \psi}{\partial z}, \quad w = -\frac{\partial \psi}{\partial x}, \quad \omega = -\nabla^2 \psi \quad (2.2)$$

the full equations, with the usual Boussinesq approximation, are given by:

$$Pr^{-1} \left(\frac{\partial \omega}{\partial t} + J(\omega, \psi) \right) = \nabla^2 \omega + Ra_T \left(\frac{\partial T}{\partial x} - R \frac{\partial S}{\partial x} \right) \quad (2.3)$$

$$\frac{\partial T}{\partial t} + J(T, \psi) = \nabla^2 T \quad (2.4)$$

$$\frac{\partial S}{\partial t} + J(S, \psi) = Le^{-1} \nabla^2 S \quad (2.5)$$

where the Jacobian J is defined as

$$J(a, b) = \frac{\partial a}{\partial x} \frac{\partial b}{\partial z} - \frac{\partial a}{\partial z} \frac{\partial b}{\partial x} \quad (2.6)$$

At all boundaries no-slip conditions for velocity are prescribed and for the temperature and salinity the following boundary conditions hold.

$$x = 0 : T = -\frac{1}{2}; \frac{\partial S}{\partial x} = 0, \quad x = A : T = \frac{1}{2}, \frac{\partial S}{\partial x} = 0, \quad (2.7)$$

$$z = 0 : S = 1, \frac{\partial T}{\partial z} = 0; \quad z = 1 : S = 0, \frac{\partial T}{\partial z} = 0. \quad (2.8)$$

The dimensionless parameters which appear in the equations above are defined as

$$Ra_T = \frac{g\alpha\Delta TH^3}{\nu\kappa_T}, \quad R = \frac{\beta\Delta S}{\alpha\Delta T}, \quad Pr = \frac{\nu}{\kappa_T}, \quad Le = \frac{\kappa_T}{\kappa_S}, \quad A = \frac{L}{H} \quad (2.9)$$

and the solutal Rayleigh number is given by

$$Ra_S = Ra_T R = \frac{g\beta\Delta SH^3}{\nu\kappa_T} \quad (2.10)$$

A relation between the Rayleigh numbers Ra_η , used in *Chen et al.* [1971], and Ra_T is $Ra_\eta = Ra_T/(R)^3$. Using $\partial S_0/\partial z = \Delta S/H$, a straightforward relation exists between the lengthscales H , η and the buoyancy ratio, i.e. $H/\eta = R$. In a liquid layer of height H , solutions with characteristic length scale η therefore correspond to R cells.

The equations and boundary conditions were discretized using a finite volume finite difference method as in *Dijkstra* [1992]. We use three types of numerical codes to study steady and transient solutions of the system of equations above. Steady states and their linear stability are calculated as a function of parameters using the continuation code presented in *Dijkstra* [1995]. A non-equidistant grid was used near the vertical boundaries in order to get an accurate representation of boundary layers. No stretching was applied in z because, in addition to the boundary layers at the horizontal walls, also large internal vertical gradients, in particular in salinity, may occur.

Two time-dependent numerical solvers, an explicit code using a fast Poisson solver and an fully implicit solver, were used. The first code has the advantage that it can be run at high resolution. However, its disadvantage is the restriction of the time step because of numerical instability. With the second code larger time steps can be taken but at lower resolution. Hence, the explicit code was used in the initial stage of the development of the flow and the implicit code in the approach to steady state. The codes were verified using standard problems and the choice of resolution and time step was based on extensive testing of the accuracy of the solutions.

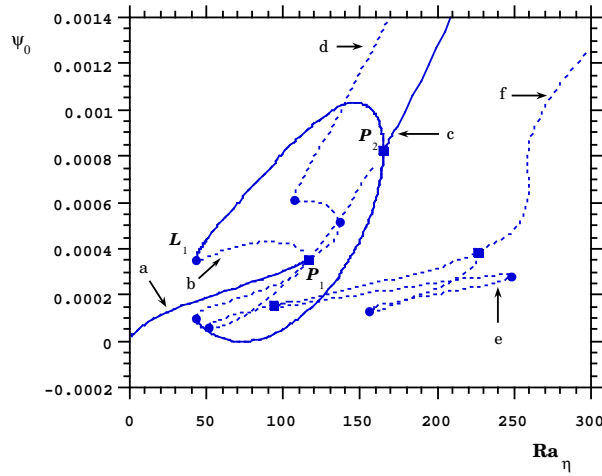


Figure 2.1: Bifurcation diagram for $R = 3$ at small Ra_η . Note that the unstable branch starting at P_2 is not connected to P_1 ; the crossing is a visual effect caused by the particular choice of the monitor function.

2.3 Results for the unicellular flow regime: $R = 3$

The Prandtl and Lewis numbers are fixed at values corresponding to the heat/salt system: $Pr = 6.7$, $Le = 101$ and the aspect-ratio A is fixed at $A = 1/2$. In a typical experiment in the unicellular flow regime, regime IV in *Lee et al.* [1990], first a 4-cell pattern is observed, thereafter cells merge until a 2-cell state is reached and finally a 1-cell solution is obtained, which appears to be a steady state of the system. In this section, we first determine the steady states of the system and subsequently study the time evolution towards the stable steady states.

2.3.1 Branches of steady solutions

In these computations, we choose Ra_η as the bifurcation parameter; when this parameter is varied, both Ra_T and Ra_S vary. In Fig. 2.1 the bifurcation diagram for $R = 3$ is shown for relatively small Ra_η ; this figure was computed using a $25 * 41$ grid. On the vertical axis, a value of the streamfunction at a particular gridpoint (ψ_0) is plotted, chosen to clearly distinguish the different solution branches. Drawn (dotted) lines indicate stable (unstable) branches and bifurcation points are indicated by markers. A square is a pitchfork bifurcation and a dot indicates a limit point. At labelled points along the branches in Fig. 2.1, plots of the streamfunction

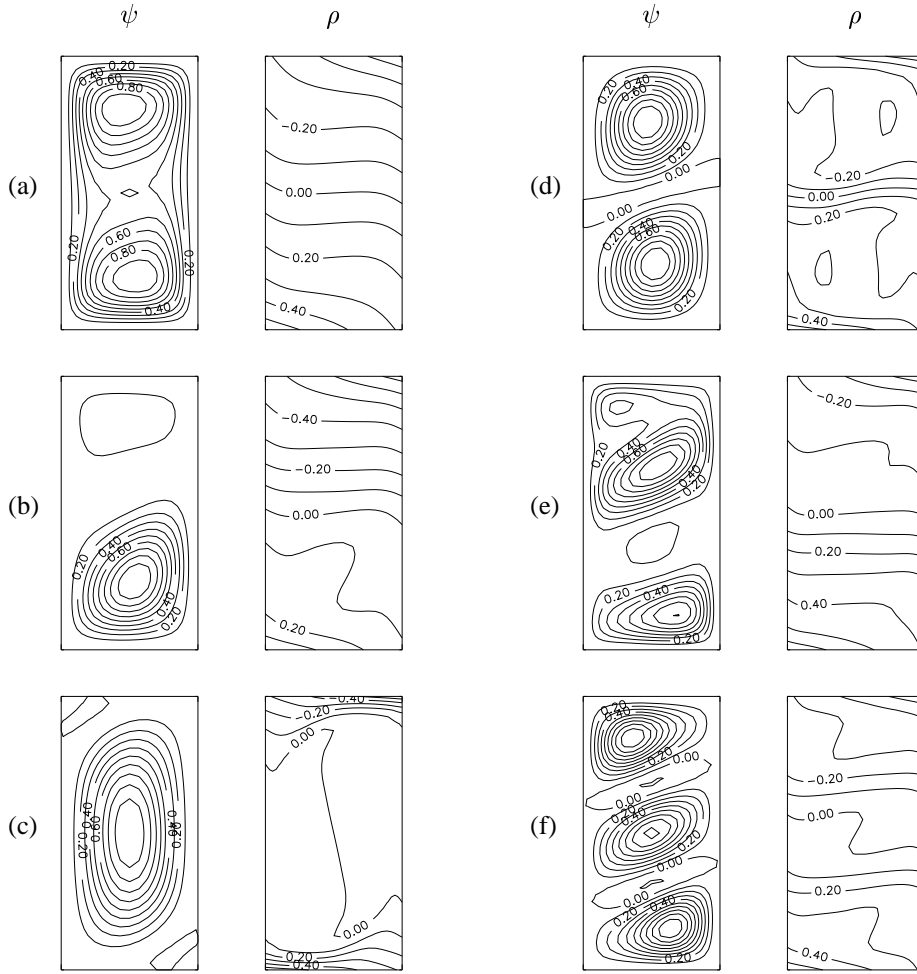


Figure 2.2: Contour plots of the streamfunction and density at selected points in Fig. 2.1. For the density the value at the center is subtracted first. All contour levels are with respect to the maximum of the field.

and density are shown in Fig. 2.2, where the dimensionless density ρ is computed as $\rho = Ra_T(RS - T)$.

When Ra_η is smaller than the value at L_1 in Fig. 2.1, there is a unique stable steady state consisting of two cells (Fig. 2.2a), which rotate in the same direction (counterclockwise). With

2. A bifurcation study of double-diffusive flows

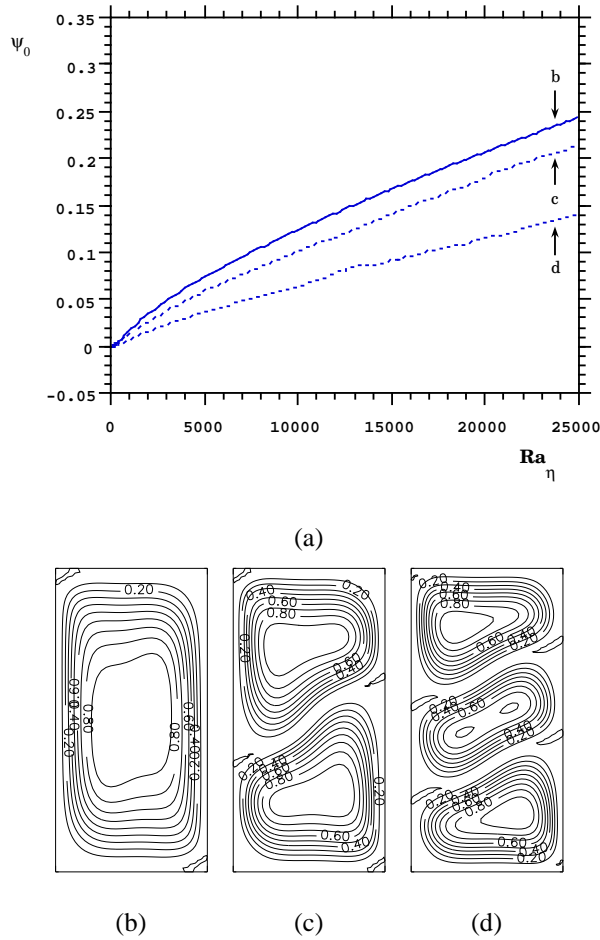


Figure 2.3: *Bifurcation diagram similar to that in Fig. 2.1 for $R = 3$ at large Ra_η . b-d. Flow patterns at selected points in Fig. 2.3a.*

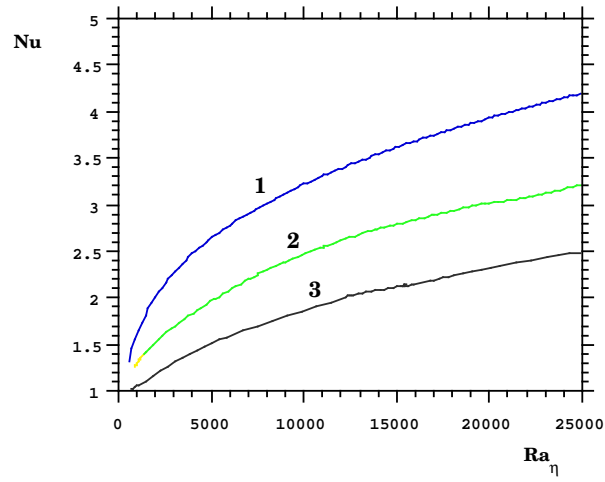
increasing Ra_η , this 2-cell pattern becomes unstable through a subcritical pitchfork bifurcation at the point labelled P_1 . This bifurcation is symmetry breaking and two branches of asymmetric solutions – but related through point-symmetry about the center of the cavity – appear. One of these solutions, a mixed 1-cell/2-cell pattern, is shown in Fig. 2.2b. Both asymmetric patterns remain unstable up to the limit point L_1 , but stabilize with increasing Ra_η and remain stable up to the bifurcation point P_2 . Along the branch $L_1 - P_2$, the flow pattern changes from a 2-cell to

a 1-cell solution. For values of Ra_η larger than at P_2 , the 1-cell pattern is the only stable pattern (Fig. 2.2c). The density is nearly homogeneous in the center of container and there is a region of weakly (statically) unstable stratification. Along the symmetric branch which continues from P_1 , the 2-cell pattern is unstable. At larger Ra_η , both cells become separated by a relatively sharp interface, most clearly seen in the density distribution (Fig. 2.2d). Within each cell, the density is nearly constant in the central region, while large gradients appear near the top and bottom. In regions of upward flow, advective salt transport increases the density upwards, causing smaller gradients downstream, but larger ones upstream. In regions of downward flow, just the opposite occurs.

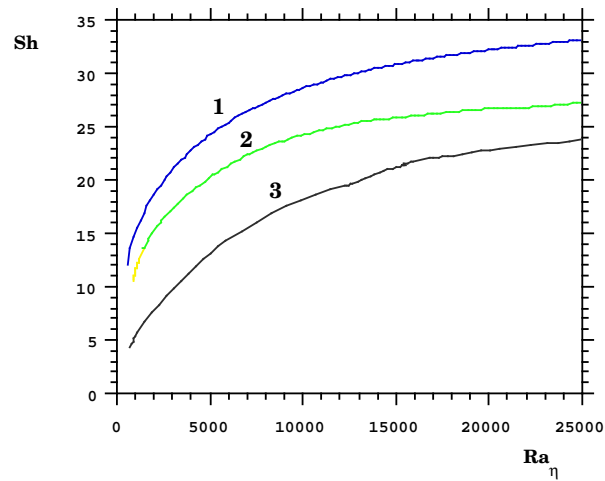
The branch coming down from P_2 also remains unstable. Along this branch, there are two other symmetry breaking bifurcation points. Here a curve of asymmetric solutions, an example shown in Fig. 2.2e appears; only one of these symmetry related branches is shown in Fig. 2.1. Along the symmetric branch, patterns appear with a slightly larger tilt and more cells at larger Ra_η . An example of a 3-cell pattern, sandwiching two small cells, is shown in Fig. 2.2f. The corresponding density plot shows that the regions of large gradients have disappeared indicating that the temperature determines the spatial pattern of the density and that the salt is well mixed (except at top and bottom). The tilt in the cells is caused by double diffusion; when the liquid moves away from the right (hot) wall, it loses its heat faster than its salt and therefore becomes heavier as the left wall is approached. The patterns along this part of the symmetric branch are all unstable.

In the small Ra_η regime there are multiple stable steady states over an interval $L_1 - P_2$ and unique stable steady states exist outside this interval (Fig. 2.1). Three branches extend into the region of larger Ra_η without any change in stability (Fig. 2.3a). The gradients in both velocity (Fig. 2.3b-d) and density become stronger and more concentrated near the boundaries of a cell, including the interfaces between the cells. The salt is well mixed within each cell and very sharp salt gradients appear at the interfaces giving a characteristic step structure in the vertical.

The increase in heat and salt transport due to convection, was monitored by calculating the Nusselt number $Nu = \int_0^1 \partial T / \partial x dz$ based on the heat flux through the vertical walls and Sherwood number $Sh = A^{-1} \int_0^A \partial S / \partial z dx$ based on the salt flux through the horizontal walls. It appeared that both quantities are constant over the layer within 1% as should be for steady flow. Generally, transport increases (Fig. 2.4a,b) with Ra_η because, at constant R , Ra_η controls the total buoyant forcing. The numbers along the branches in the Figs. 2.4 refer to the number of cells in the solution. As the number of cells increases they become smaller, allowing less vertical salt transfer because convection occurs on a smaller scale; this results in lower Sherwood numbers (Fig. 2.4b). With an increasing number of cells, the heat gain at the hot wall also decreases



(a)



(b)

Figure 2.4: Plot of the Nusselt number Nu (4a) and Sherwood number Sh (4b) as a function of Ra_η along the branches of Fig. 2.3a.

which leads to a smaller horizontal heat transport resulting in a smaller Nusselt number (Fig. 2.4a).

Although there may be more branches of steady states which do not connect to ones in the small forcing regime, a relatively simple bifurcation structure is found over a whole range of Ra_η (At least up to $Ra_\eta = 2.5 \cdot 10^4$, in an oceanographic context Ra_η is much larger: $Ra_\eta = O(10^9)$). There is only one stable pattern, the 1-cell solution, and one would expect long-term time-dependent calculations to approach this solution. This is in agreement with numerical results in *Lee and Hyun* [1991], where a 1-cell pattern was found for $R = 3$ and $Ra_T = 8.0 \cdot 10^7$ (corresponding to $Ra_\eta = 2.96 \cdot 10^6$). It is also in agreement with experimental results in *Lee et al.* [1990] since the parameters here belong to those characterizing regime IV.

2.3.2 Evolution towards steady state

The evolution of the flow in the cavity is studied from an initially motionless isothermal liquid which is stably (salt) stratified. At $t = 0$ a constant horizontal temperature difference is imposed. The initial conditions are

$$t \leq 0 : \quad \psi = \omega = 0; \quad S = 1 - z \quad (2.11)$$

$$t < 0 : \quad T = 0 \quad (2.12)$$

$$t = 0 : \quad T(x = 0) = -\frac{1}{2}; \quad T(x = A) = \frac{1}{2} \quad (2.13)$$

and are compatible with all boundary conditions. The $25 * 41$ grid used to determine the steady states in Fig. 2.3 proved to be too coarse, because during the initial evolution smaller scale patterns appeared. It turned out that a $49 * 81$ grid gave sufficiently accurate results in that doubling the spatial resolution and halving the time step did not show much difference over a chosen time interval. This grid size is comparable to that used in *Lee and Hyun* [1991].

For $Ra_\eta = 2.37 \cdot 10^4$ the evolution monitored by the maximum of the streamfunction ψ_m shows three different stages (Fig. 2.5). In the first stage, a four cell solution (Fig. 2.6a) is reached in a relatively short time. The vertical length scale of the convection cells is slightly smaller than η . Consistent with Fig. 2.3a, where no 4-cell stable steady solution was found, two pairs of cells merge as time progresses and a 2-cell pattern forms (Fig. 2.6b). Both the flow pattern and the corresponding density field hardly change over a long time interval (Fig. 2.5). However, the integration was continued, because no stable 2-cell pattern was found in Fig. 2.3a. Eventually, indeed the 2-cell pattern becomes unstable, weakening the lower cell (Fig. 2.6c) and relatively quickly the 1-cell pattern (Fig. 2.6d) is reached which remains steady, consistent with Fig. 2.3a.

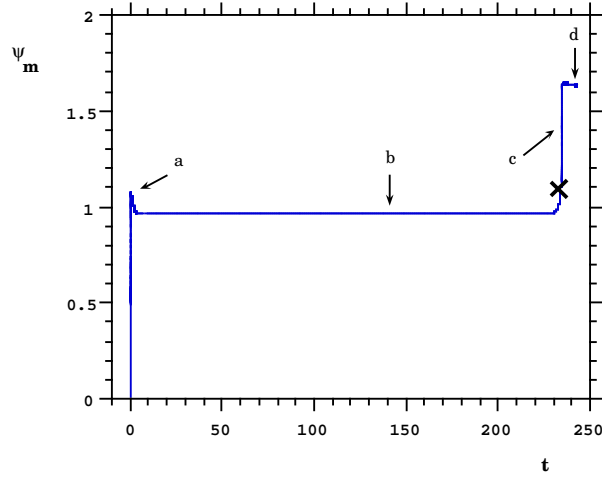


Figure 2.5: Maximum of the streamfunction as a function of time for $R = 3$ and $Ra_\eta = 2.37 \cdot 10^4$.

At $t = 0$ a discontinuity in the temperature distribution at the vertical boundaries occurs. Since Nu is evaluated at the vertical boundaries, it is not defined at $t = 0$. As the 4-cell pattern is formed, Nu quickly falls to a value of about 1.9. Subsequent transitions, leading to the 2-cell and the final 1-cell pattern, cause Nu to increase for reasons described above. Similarly, the Sherwood number increases with each transition to less cells. The final values of Nu and Sh for the 2-cell and 1-cell solutions agree well with the values that can be obtained from Fig. 2.4 at $Ra_\eta = 2.37 \cdot 10^4$. Small differences in the numerical values occur because of the different grid sizes used in the calculations (25×41 for the calculation of the steady branches and 49×81 for the time dependent results).

The correspondence between the 2-cell pattern in Fig. 2.3c and Fig. 2.6b is striking. Actually, the time dependent 2-cell solution proved to be a very close approximation to the steady-state solution at the 2-cell branch in Fig. 2.3a. Using the former as a steady-state approximation for the continuation method, a steady state was reached within three Newton iterations. From Fig. 2.5 it can be seen that the unstable 2-cell solution is physically relevant, because it will be observed for a long time. Since time is scaled with the thermal diffusion time, which is in the order of a day for typical experimental configurations, the 2-cell solution may be present for a much longer time-period. i.e. about $100H^2/\kappa_T[s]$. As the salt diffusion time scale $\tau_S = H^2/\kappa_S$ based on the height of the container has this order of magnitude, the instability of the 2-cell steady solution in Fig. 2.3c is likely to be related to intercellular salt diffusion. In Fig. 2.7 the vertical profile of the

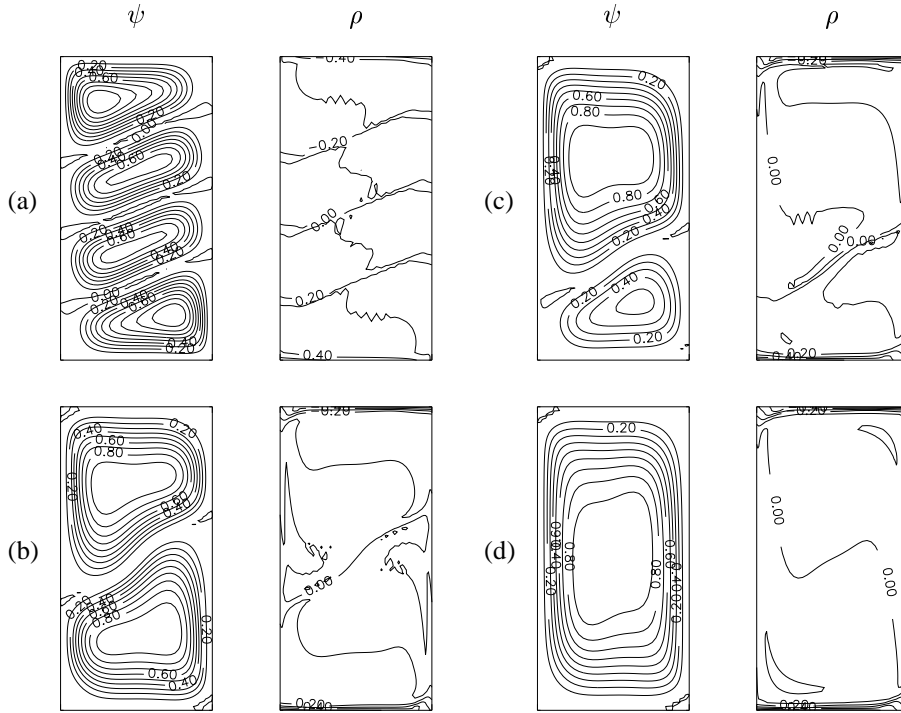


Figure 2.6: Plot of the stream function and the density at selected points in Fig. 2.5.

salt field ($S(A/2, z)$) at the middle of the container is shown both for the 2-cell unstable steady state (drawn line) and at the marked point in Fig. 2.5 (dotted line). Indeed, the characteristic length scale over which the salinity difference between both layers exists is of the order H .

However, when the growth factor ($\lambda = 6.78 \cdot 10^{-2}$) – calculated by solving the linear stability problem of the 2-cell steady state – is considered, this value gives a time scale much smaller than τ_S . What actually happens is observed from the flow pattern of the most unstable mode (Fig. 2.8a) and the difference between the time dependent flow and the 2-cell steady solution (Fig. 2.8b - c) at different times. At the beginning of the quasi-steady regime, the difference solution (Fig. 2.8b) contains more modes than the most unstable mode, in particular a 4-cell pattern. It appears that a long preconditioning phase is necessary to filter out the components of the stable modes. Once these modes have decreased in magnitude (Fig. 2.8c), the instability of the 2-cell flow pattern sets in. This instability occurs indeed on a time scale set by λ as was confirmed by perturbing the 2-cell steady state with the unstable mode of very small positive amplitude

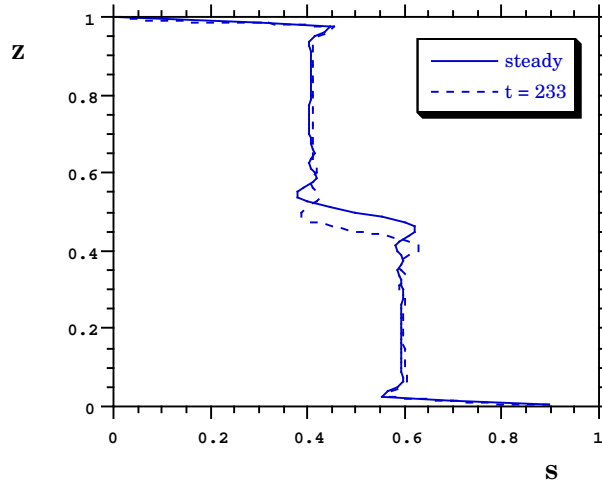


Figure 2.7: Vertical profile of the salinity field $S(A/2, z)$ for the 2-cell steady state of Fig. 2.3c and that of the time-dependent state at the marked point in Fig. 2.5.

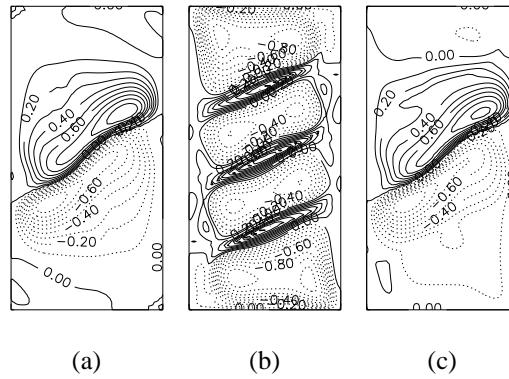


Figure 2.8: a. Plot of the streamfunction of the eigenvector corresponding to the most unstable mode of the 2-cell branch ($Ra_\eta = 2.37 \cdot 10^4$). b. Difference of the streamfunction of the transient state at $t = 7.92$ and the steady state. c. Same as b. but at $t = 2.29 \cdot 10^2$.

and following the evolution by time integration. Exponential growth was observed immediately; the growth factor was computed as $6.95 \cdot 10^{-2}$, very close to the value of λ . If one perturbs the steady state with the same perturbation pattern but with a negative amplitude (this is also an eigenvector), the same instability develops and the lower cell is strengthened.

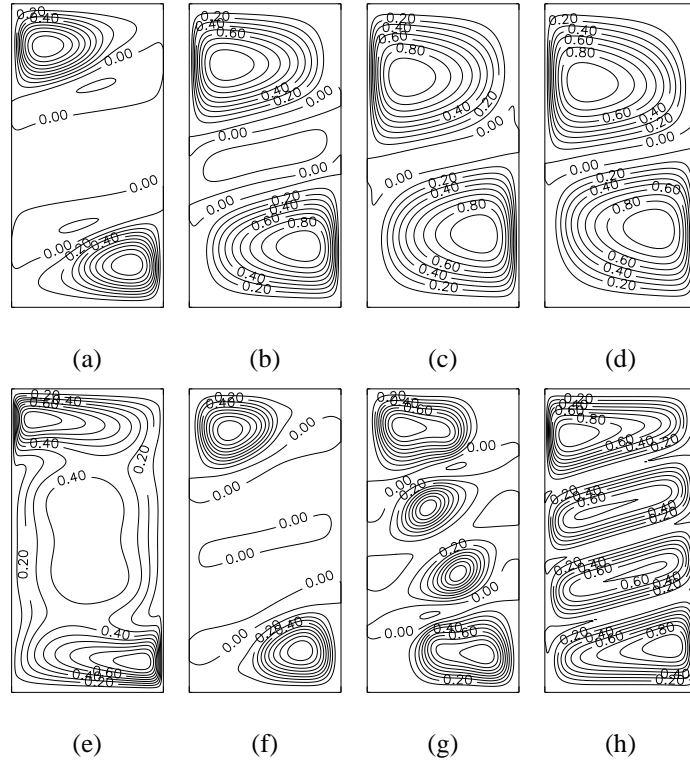


Figure 2.9: Comparison of initial flow development for small $Ra_\eta = 5.0 \cdot 10^3$ (panels a-d) and larger $Ra_\eta = 2.37 \cdot 10^4$ (panels e-h).

The flow development as described above depends on the value of Ra_η . We performed another transient run, at much smaller $Ra_\eta = 5.0 \cdot 10^3$. In Fig. 2.9, a comparison between small and large Rayleigh number initial flow development is shown as a sequence of plots of the streamfunction. At small Ra_η , convection cells form at the lower and upper wall and spread out into the cavity (Fig. 2.9a-d). Further integration in time shows that a 2-cell solution appears which approaches the unstable 2-cell steady solution (as in Fig. 2.3c). At large Ra_η , two cells form in the center and the two cells close to the horizontal walls (Fig. 2.9e-h) do not extend downward. The time scale for which the evolution in Fig. 2.9a-d is shown is about a factor 10 slower than that of the development shown in Fig. 2.9e-h. Clearly, the main difference between the large and small Rayleigh number transients is the appearance of the 4-cell state.

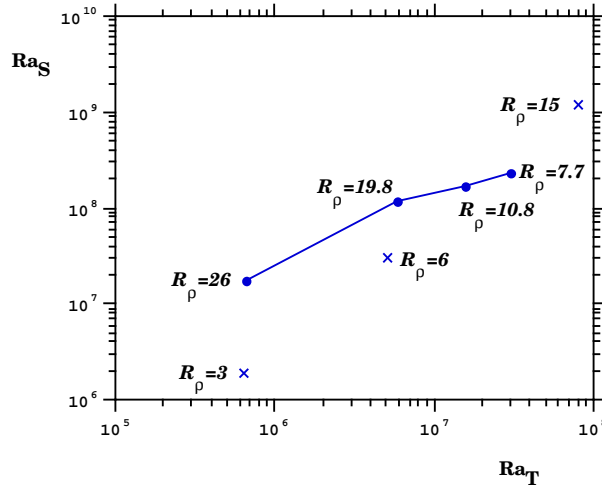


Figure 2.10: Path of the bifurcation point corresponding to the instability of the unicellular flow. Also indicated are the locations where trajectories were computed (crosses).

2.4 Boundaries between different flow regimes

In *Lee et al.* [1990] it was shown that in a container with the same boundary conditions and aspect-ratio as used in our model, different steady state flow regimes exist depending on the values of Ra_T and R . In this section, we try to identify the boundaries between the qualitatively different flow regimes as paths of particular bifurcation points of the underlying dynamical system.

For example, the results in *Lee et al.* [1990] suggest that the unicellular thermally dominated solution no longer exists at larger buoyancy ratio, where cells form simultaneously. A boundary between regimes III (the simultaneously formed layer flow regime) and IV (the unicellular flow regime) apparently exists. We will approach this boundary from the results in Fig. 2.3a, where three solution branches were computed up to very large Ra_η . At four fixed values of Ra_T , the flow pattern at the 1-cell branch was continued up to larger Ra_S , thereby increasing the buoyancy ratio. For each of these cases, the unicellular flow becomes unstable at a critical value of the buoyancy ratio through a pitchfork bifurcation. The path of this bifurcation in the (Ra_T, Ra_S) plane is plotted in Fig. 2.10. At larger Ra_T , the value of the buoyancy ratio is of the order 10, which is reasonably in agreement with the experiments in *Lee et al.* [1990]. This value may depend on the Lewis number, actually it is close the square root of it, but this is not further explored here. The result in Fig. 2.10 strongly supports that the boundary between region III and

IV can be identified as the instability of the unicellular flow.

However, even in the unicellular flow regime, layered flow patterns with a much smaller scale may be observed for a long time. As an example we present (Fig. 2.11) the transient flow for $R = 6$ and again $Ra_\eta = 2.37 \cdot 10^4$. The location of the trajectory in the (Ra_T, Ra_S) plane is also indicated in Fig. 2.10. A flow pattern with vertical lengthscale η appears after some time, but changes into a 4-cell solution. The vertical distribution of fluid properties in the 4-cell solution compares qualitatively well with the case of $R = 3$: convection cells are separated by thin interfaces.

To the left of the drawn curve in Fig. 2.10, the 1-cell solutions no longer exist as stable steady states. When the points on the curve are continued towards smaller values of Ra_T , while fixing Ra_S , region III is explored. The buoyancy ratio is increased further along this path in parameter space. However, along each path computed, an enormous amount of bifurcation points and limit points appear, similar to that found in the small buoyancy ratio regime at large Ra_S [Tsitverblit and Kit, 1993; Kranenborg and Dijkstra, 1995; Tsitverblit, 1995]. Computationally, it became too expensive to investigate these bifurcation structures in detail. However, the results in Kranenborg and Dijkstra [1995] suggest that indeed multicellular flow patterns may exist as steady states. These states appear due to a combined effect of advection of salt and the appearance of stagnant flow regions when the forcing decreases which are filled up with cells when the forcing increases. These states may be unstable, as in Kranenborg and Dijkstra [1995], but they might be physically relevant, because also a preconditioning mechanism may be necessary for the instability to occur. With respect to the steady state structure, regimes II and III cannot be clearly distinguished since solution branches corresponding to both regimes likely exist in the same region of parameter space.

Characteristic of the patterns found in regime II is their asymmetry with respect to the center of the cavity [Lee *et al.*, 1990]. This indicates that these patterns are associated with asymmetric branches, appearing through symmetry breaking bifurcations from the symmetric branch. As an example of such an asymmetric pattern, the evolution of the flow for $R = 15$ and $Ra_\eta = 2.37 \cdot 10^4$ is shown in Fig. 2.12. The location of the trajectory in the (Ra_T, Ra_S) plane (indicated in Fig. 2.10) is certainly to the left of the curve bounding the unicellular flow regime. The numerical resolution of this particular simulation was increased to a 50×100 grid (and the initial stages were checked with grids up to 150×300), because small scale structures appear during the initial stages of evolution. Even with this high resolution, the flow development is quite irregular (Fig. 2.12a) and certainly no steady state has been reached at the end of the computation. The evolution of the flow pattern (Fig. 2.12b-e) is similar to the one observed in Lee *et al.* [1990] in the successively formed layer flow regime. Cells appear near upper and lower boundary, where well mixed layers

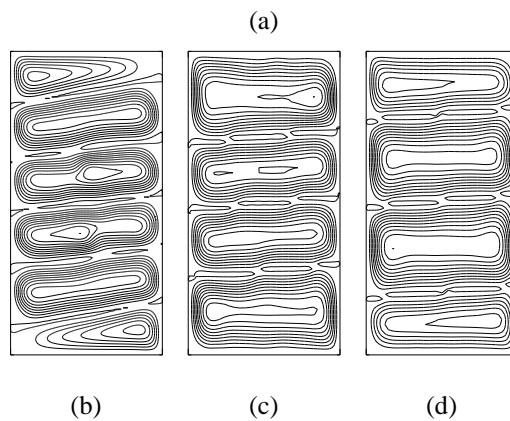
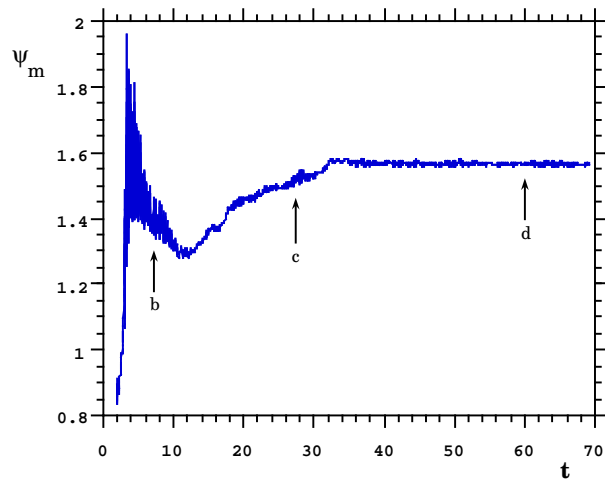


Figure 2.11: *a.* Plot of the maximum of ψ as a function of time for $R = 6$ and $Ra_\eta = 2.37 \cdot 10^4$. *b-d.* Flow patterns at selected points in Fig. 2.11a.

develop. At first these cells appear symmetrically, but later an asymmetry develops as also seen in experiments. The lower cell remains well mixed as a whole whereas in the upper area two separate layers develop.

According to the experiments in *Lee et al.* [1990], regime I is characterized by a very weak flow concentrated near the horizontal walls. This weak flow is similar to that on the primary solution branch (Fig. 2.1 and Fig. 2.2a), which is obtained by continuation of the zero flow

2.4. Boundaries between different flow regimes

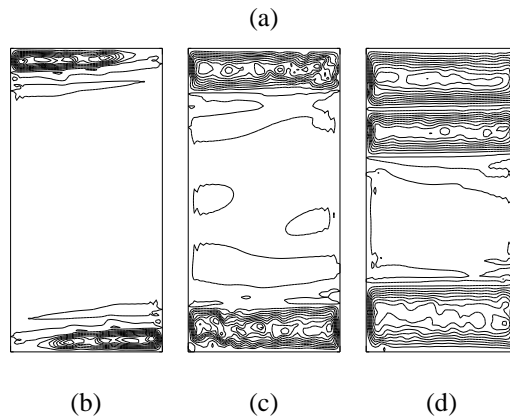
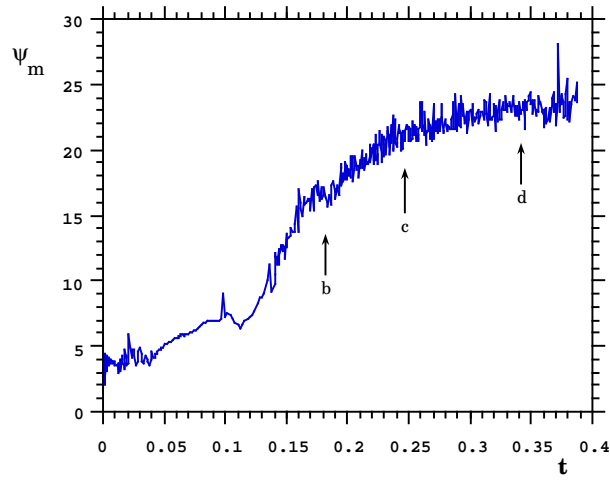


Figure 2.12: Same as Fig. 2.11, but for $R = 15$.

solution to larger thermal forcing. As regime II is associated with the occurrence of asymmetric solutions, the limit point L_1 in Fig. 2.1 is a good candidate as a boundary of different qualitative behavior since below this point, only symmetric solutions exist. However, because of the large computational effort we have not followed the path of the limit point in parameter space.

2.5 Discussion

In this chapter, we attempted to identify the different flow regimes as found in experiments of *Lee et al.* [1990] by paths of bifurcation points of the governing system of differential equations. This has been partly successful since basically only the boundary between region III and IV can be clearly identified and a good guess is obtained for that between region I and II. The boundary between regimes II and III is not that clearly defined because of the abundance of bifurcation points in this area of parameter space. The precise reason for this is unclear but apparently the symmetric flow is very sensitive to asymmetric perturbations.

However, many interesting results have been obtained during this attempt. Above some critical value of Ra_η associated with the limit point marking the boundary between regimes I and II, multiple steady states were found over a large region of parameter space. In regime IV, the low buoyancy ratio regime, the structure of attractors is quite simple since only three branches extend to very large Ra_η . The evolution of the flow towards the unicellular stable flow was shown to remain for a long time near one of the unstable states before it undergoes an instability. This means that the unstable states are physically relevant since they may be observed for a very long time. In principle, this instability can be due to the shear in the basic state or it can be buoyancy driven, whereby double diffusion may play a role. To investigate whether shear might be a candidate, the Richardson number defined by $Ri = -\frac{\partial \rho}{\partial z} / \frac{\partial u^2}{\partial z}$ where u denotes the horizontal component of the velocity was computed. The values of Ri near the interface between the two cells (Fig. 2.6b) are quite large (> 1). Hence, it is unlikely that shear will drive the instability. Also the structure of the most unstable mode (Fig. 2.8a) does not suggest a shear driven instability, since smaller perturbation structures would be expected.

It turns out to be difficult to show why the most unstable mode, as in Fig. 2.8a, and the corresponding perturbations in the other quantities get amplified through a buoyancy driven mechanism. However, when the flow perturbation (Fig. 2.8a) is superposed on the steady state flow (Fig. 2.3c), the upper cell gets amplified, and the intensity of the lower cell is diminished. Hence, there will also be asymmetric transport of heat and salt and apparently this leads to amplification of the perturbations. During the transition from the 2-cell solution to the final 1-cell solution, there is little sign of interface breakdown, at least not in the early stages of the transition. As the interface migrates downwards, both the strength of the salinity gradient and the thickness of the interface remain nearly the same (Fig. 2.7).

Even when the parameters are chosen in the unicellular flow regime, it should be stressed that for large enough Ra_T , cellular structures with lengthscales much smaller than that of the container size may be observed for a long time. In other words, signatures of regime III may already be present in the trajectories in regime IV. These patterns likely are related to unstable

steady states just as in the case $R = 3$. Similarly, at small Ra_T signatures of the successively formed flow regime can be found in the trajectories in regime IV. Hence, these results indicate that it should be difficult to distinguish the different flow regimes experimentally, in particular the boundary between the regions II and III. Indeed, *Lee et al.* [1990] and *Chen et al.* [1971] give overlapping intervals for the buoyancy ratio corresponding to the two regimes. The critical value of Ra_η as proposed by *Chen et al.* [1971] cannot be identified here as a path of a particular bifurcation point.

The boundary between region I and II is likely to be related to the appearance of the limit point on the asymmetric branches appearing from the first pitchfork bifurcation. One might ask, whether this pitchfork bifurcation is related to the double diffusive instability of a parallel flow in the limit of a vertically unbounded layer *Thangam et al.* [1981]. With $A = 1/2$ the steady state solutions near this pitchfork are not a good approximation to the parallel flow in an infinite vertical slot. We followed the path of the primary bifurcation point (P_1 in Fig. 2.1) towards smaller A , and although the steady state flow became more and more parallel, the primary bifurcation was always to an asymmetric state and not to an array of cells. These results clearly show that the primary bifurcation point and the point of instability of the parallel flow in a narrow slot are not clearly related; the upper and lower walls appear to play a dominant role in the instability of the flow.

As a summary, it appears that the underlying dynamical structure of the attractors in this particular case does not help to understand the observed flow patterns as much as one could hope for. Several aspects of the flow in experiments, other than in *Lee et al.* [1990], are neglected in this study such as impervious horizontal walls and a time - dependent heating function at the sidewall. The influence of these aspects can only be studied by direct numerical simulation using a high resolution. Although in this case, only steady patterns exist for which the salt is homogeneous, it is expected that the attractors computed with fixed salt field at top and bottom 'deform' to slow regions in phase space. In this case, the patterns found above (e.g. the unicellular flow), may appear as quasi-steady states. However, certainly at higher buoyancy forcing, very complicated trajectories can be expected; work on this is currently in progress.

References

- Akbarzadeh, A., Manins, P., Convective layers generated by side walls in solar ponds, *Solar Energy*, **41**(6), 521–529 (1988).
- Chen, C. F., Briggs, D. G., Wirtz, R. A., Stability of thermal convection in a salinity gradient due to lateral heating, *Int. J. Heat Mass Transfer*, **14**, 57–65 (1971).
- Dijkstra, H.A., On the structure of cellular solutions in Rayleigh-Bénard-Marangoni flows in small-aspect-ratio containers, *J. Fluid Mech.*, **243**, 73-102 (1992).
- Dijkstra, H.A., Molemaker, M.J., Van der Ploeg, A., Botta, E.F.F., An efficient code to compute non-parallel flows and their linear stability, *Computers & Fluids*, **24**(4), 415–434 (1995).
- Fernando, H. J. S., Brandt, A., Recent advances in double-diffusive convection, *Appl. Mech. Rev.*, **47**(9), C1–C7 (1995).
- Huppert, H. E., Turner, J. S., Ice blocks melting into a salinity gradient *J. Fluid Mech.*, **100**, 367–384 (1980).
- Jeevaraj, C., Imberger, J., Experimental study of double-diffusive instability in sidewall heating, *J. Fluid Mech.*, **222**, 565–586 (1991).
- Kerr, O. S., Heating a salinity gradient from a vertical sidewall: linear theory, *J. Fluid Mech.*, **207**, 323–352 (1989).
- Kerr, O. S., Heating a salinity gradient from a vertical sidewall: nonlinear theory, *J. Fluid Mech.*, **217**, 529–546 (1990).
- Kranenborg, E. J., Dijkstra, H. A., The structure of (linearly) stable double diffusive flow patterns in a laterally heated stratified liquid, *Physics of Fluids*, **7**(3), 680–682 (1995).

REFERENCES

- Lee, J. W, Hyun, M. T. & Kang, Y.S., Combined natural convection due to lateral heating in a stably stratified solution, *Int. J. Heat Mass Transfer* **33**, 869–875 (1990).
- Lee, J. W. & Hyun, J. M., Double diffusive convection in a cavity under a vertical solutal gradient and a horizontal temperature gradient, *Int. J. Heat Mass Transfer*, **34**, 2423–2427 (1991).
- Schmitt, R.W., Double diffusion in oceanography, *Ann. Rev. Fluid Mech.*, **26**, 255-285 (1994).
- Tanny, J., Tsinober, A. B., The dynamics and structure of double-diffusive layers in sidewall-heating experiments, *J. Fluid Mech.*, **196**, 135–156 (1988).
- Thangam, S., Zebib, A. & Chen, C. F., Transition from shear to sideways diffusive instability in a vertical slot, *J. Fluid Mech.*, **112**, 151–160 (1981).
- Thorpe, S.A., Hutt, P.K., Soulsby, R., The effect of horizontal gradients on thermohaline convection, *J. Fluid Mech.*, **38**, 375-400 (1969).
- Tsitverblit, N., Bifurcation phenomena in confined thermosolutal convection with lateral heating: Commencement of the double-diffusive region, *Physics Fluids A.*, **7**, 718–736 (1995).
- Tsitverblit, N., Kit, E., The multiplicity of steady flows in confined double-diffusive convection with lateral heating, *Physics Fluids A.*, **5**, 1062–1064 (1993).
- Wirtz, R. A., Briggs, D. G., Chen, C. F., Physical and numerical experiments on layered convection in a density–stratified fluid, *Geophysical Fluid Dynamics* , **3**, 265–288 (1972).